

# The Living With a Star Space Environment Testbed Payload

C.S. Dyer, K.A. Ryden, P.A. Morris, A.D.P. Hands, P.J. McNulty, J-R. Vaille, L. Dusseau, G. Cellere, A. Paccagnella, H.J. Barnaby, A.R. Benedetto, R. Velazco, R. Possamai Bastos, D. Brewer, J.L. Barth, K.A. LaBel, M.J. Campola, Y. Zheng, and M.A. Xapsos

**Abstract**— The objectives, instrumentation, methods and data leading up to launch of the NASA Living With a Star (LWS) Space Environment Testbed (SET) payload onboard the Air Force Research Laboratory Demonstration and Science Experiments (DSX) spacecraft are described. The experiments characterize the space radiation environment and how it affects hardware performance. The payload consists of a compact space weather instrument and a carrier containing four board experiments.

**Index Terms**— Demonstration and Science Experiments (DSX), galactic cosmic rays, Living With a Star (LWS), solar energetic particles, Space Environment Testbed (SET), Van Allen belts.

## I. INTRODUCTION

THE NASA Living With a Star (LWS) program provides missions to improve our understanding of space weather and space climate; how the Earth and solar system respond; and how humanity is affected. Within LWS, the Space Environment Testbed (SET) program selected a payload to characterize the space radiation environment in Medium Earth Orbit (MEO) and how it affects hardware performance. The overall goal is to improve spacecraft design, engineering and operations [1].

The SET payload studies hazards present for devices and integrated circuits in space systems and instrumentation. The focus is three categories of high-energy particle radiations. The first is particles trapped in the Earth's magnetic field, the Van Allen belts. The second is galactic cosmic rays, comparatively low-level but extremely energetic ions that originate outside of our solar system. The third is solar particle events, i.e., coronal

mass ejections and solar flares, characterized by high intensity periods of protons and heavy ions. Underestimating these radiation levels leads to excessive risk and can result in degraded system performance and loss of mission lifetime. Overestimating the radiation levels can lead to use of excessive shielding, reduced payloads, over-design and increased cost. The pervasive use of commercial-off-the-shelf (COTS) microelectronics in spacecraft to achieve increased system performance must be balanced by the need to accurately predict their complex responses in space, which begins by understanding the environment in which they function. A summary of space radiation models used for spacecraft design is given in [2]. Proposed metrics for these radiations are given in [3].

Radiation effects caused by these high-energy particle radiations can generally be grouped into four categories: degradation from Total Ionizing Dose (TID), degradation from Total Non-Ionizing Dose (TNID), Single Event Effects (SEE), and Internal Charging (IC). TID and TNID effects in electronic and photonic parts result in cumulative, long-term degradation due to ionizing or non-ionizing radiation—mainly primary protons and electrons but secondary particles arising from interactions between these primary particles and spacecraft materials can also contribute. For the case of Total Ionizing Dose, the concern is mainly its effects in insulating regions of metal-oxide semiconductors (MOS) and bipolar devices, most commonly composed of SiO<sub>2</sub>. In MOS devices, ionizing radiation causes threshold voltage shifts due to exposure of gate oxides. The effect first appears as parametric degradation and can eventually result in functional failure. Ionizing radiation can also cause leakage currents in MOS devices due to exposure of field oxide regions used for isolation and result in increased power consumption. Eventually the effect becomes so pronounced that n-channel transistors cannot be switched to the off state. For bipolar devices loss in performance is caused by gain degradation and increased recombination currents. In addition, bipolar devices can be subject to the Enhanced Low Dose Rate Sensitivity (ELDRS) effect, wherein the amount of TID degradation at a given total dose level is greater at low dose rates than at high dose rates. This complicates extrapolating the effects observed in laboratory testing to the lower dose rates observed during space missions. The effects of Total Non-Ionizing Dose, also referred to as displacement damage dose, are also cumulative effects caused when the incident radiation displaces atoms in a semiconductor lattice or optical material.

Manuscript submitted Sept. 7, 2022. Revised Nov. 20, 2022.

This work was supported by the NASA Living With a Star (LWS) Space Environment Testbed (SET) Program.

C.S. Dyer is with Surrey Space Center, University of Surrey, Guildford, UK and CSDRadConsultancy, Fleet, UK

K.A. Ryden, P.A. Morris and A.D.P. Hands are with Surrey Space Center, University of Surrey, Guildford, UK

P.J. McNulty, deceased, was with the Department of Physics and Astronomy, Clemson University, Clemson, USA

J-R. Vaille and L. Dusseau are with the Centre de Microelectronics and Electronics, Universite de Montpellier, Montpellier, France

G. Cellere and A. Paccagnella are with the Department of Information Engineering, Padova University, 35100 Padova, Italy

H.J. Barnaby and A. R. Benedetto are with the School of Electrical, Computer and Energy Engineering, Arizona State University, Tempe, USA

R. Velazco and R. Possamai Bastos are with the University Grenoble Alpes, CNRS, Grenoble INP, TIMA, 38000 Grenoble, France

D. Brewer (retired) is with NASA Headquarters, Washington DC, USA

J.L. Barth\* (retired), K. LaBel^ (retired), M.J. Campola, Y. Zheng and M.A. Xapsos (retired; email: Michael.A.Xapsos@nasa.gov) are with NASA Goddard Space Flight Center, Greenbelt, MD, USA

\* Currently at Cornell Technical Services, Columbia, MD, USA

^ Currently at Science Systems & Applications Inc., Lanham, MD, USA

This produces defects that result in material property changes such as carrier lifetime shortening, mobility decreases and degradation of optical transmission. TNID effects are commonly observed in components such as solar cells, focal planes and optocouplers. It is possible to reduce total dose effects in space to a limited extent with shielding material. However, the amount of shielding that can be used is limited by weight constraints.

SEE can be defined as any measurable effect in a circuit caused by a single incident particle. It can be either non-destructive such as single event upset (SEU) and single event transients (SETs) or destructive such as single event latchup (SEL) and single event gate rupture (SEGR). The severity of the effect can range from noisy data to system shutdown, depending on the type of effect and the criticality of the system in which it occurs.

SEE can be caused by direct ionization as the incident particle passes through a sensitive region of a device. This is usually the case for incident heavy ions. The metric traditionally used to characterize the incident ion is Linear Energy Transfer (LET). LET is the ionizing energy lost by the ion per unit path length in the material of the sensitive volume of the circuit.

SEE can also be caused by nuclear reaction products from the interaction of the incident particle with a nucleus in the circuit material. This is usually the case for incident protons. For this situation single event rate analysis is more complex because there can be several emerging reaction products but the key metric for SEE in all cases is the charge deposited in the sensitive volume of the circuit.

Shielding can mitigate SEE in the Van Allen belts and from solar particle events to a limited extent. However, SEE rates due to galactic cosmic rays provide a lower limit that is not practical to get below due to their very high energy and penetrating nature.

Internal charging occurs when radiation, usually energetic electrons, causes charge buildup in dielectric materials or ungrounded conductors in the interior of spacecraft. An electrostatic discharge can occur if the local electric field strength exceeds the dielectric strength of the material or if the potential difference between the charged material and a conductive surface reaches a critical value. The discharge itself can be damaging and it can also generate spurious signals.

DSX was deployed in an elliptical orbit (perigee ~6000 km, apogee ~12000 km, inclination 42°) covering the slot region part of MEO in between the inner and outer Van Allen belts. The SET payload consists of a compact space weather instrument, the Cosmic Radiation Environment Dosimetry and Charging Experiment (CREDANCE), and a carrier containing 4 board experiments. CREDANCE consists of several sensor suites to measure the energetic particle environment. Protons and heavy ions are detected using two particle telescopes. Internal charging currents are characterized at three shielding depths using parallel aluminum plates connected to electrometers. Total ionizing dose is measured with metal-oxide-semiconductor devices at two shielding depths. Two boards contained in the carrier are for the Dosimetry

Intercomparison and Miniaturization Experiment (DIME). These boards use commercial-off-the-shelf microelectronic structures and devices to perform space dosimetry for TID and TNID, and to measure SEE and LET spectra for protons and heavy ions. These can be integrated into board designs with minimal increase in board size and power. The two other boards are focused on effects observed in devices commonly used in spacecraft. The Enhanced Low Dose Rate Sensitivity (ELDRS) experiment studies this low dose rate effect at the transistor level. It uses specially fabricated bipolar devices designed to evaluate the influence of key processing characteristics on the ELDRS effect. The Commercial Off the Shelf-2 (COTS-2) experiment will measure SEE in a Field Programmable Gate Array (FPGA). It will attempt to validate an approach to SEE rate prediction using laboratory test data and fault injection techniques. All experiments were selected through a NASA open competition [4]. The SET payload is described in more detail in the following.

## II. COSMIC RADIATION ENVIRONMENT DOSIMETRY AND CHARGING EXPERIMENT (CREDANCE)

CREDANCE measures the primary space weather environments which influence the design and in-orbit behavior of spacecraft, namely energetic protons, electrons, ions, internal charging, and total ionizing dose. CREDANCE shares many design features with the ‘Merlin’ instrument which has been operating on the Giove-A satellite since 2005 in a Global Positioning System (GPS)-like medium Earth orbit [5,6]. The sensor suites fitted to CREDANCE have evolved over a series of missions starting with CREAM and CREDO [7,8] first deployed in the late 1980s and culminating in the provision of environment data for the Microelectronics and Photonics Testbed over a seven year period. Additional sensors were added to measure electrons and charging [9,10] as well as total ionizing dose [5] in the early 2000s. The basic Merlin/CREDANCE sensor suite has since been further developed for use in the Environmental Monitoring Units (EMUs) currently operating in MEO on the European Galileo navigation fleet [11] and another two EMUs orbiting on the Japanese Himawari satellites [12] located in geostationary orbit: these concurrent missions could provide useful opportunities for direct comparison of results from different orbital regimes.

CREDANCE comprises two card-frame modules each housing one printed circuit board: the upper module accommodates the ‘sensor board’ on which the radiation detectors and their associated front-end electronics are located, a photograph of which is provided in Fig. 1. The large diameter sensor (‘SURF’) is used for measuring internal charging effects and electrons. There are two particle telescopes; one for measuring ion LET spectra and one for measuring proton fluxes. In addition two Radiation-sensing Field Effect Transistors (RadFETs) are provided for measuring accumulated total ionizing dose effects. The main capabilities of CREDANCE are summarized in Table I.

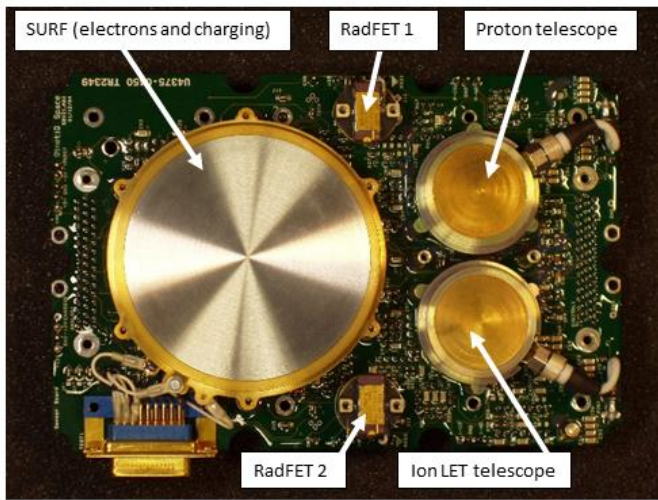


Fig. 1. CREDANCE sensors board.

TABLE I  
SUMMARY OF MEASUREMENT CAPABILITIES OF CREDANCE

Measurement Capability	
Protons	>40 MeV flux
Heavy ions	LET spectrum from 100 MeV g <sup>-1</sup> cm <sup>2</sup> to 25100 MeV g <sup>-1</sup> cm <sup>2</sup> in 32 logarithmically spaced channels
Electrons and internal charging	Internal charging currents (fA cm <sup>-2</sup> ) at three shielding depths (0.5mm, 1mm, 1.5mm Al) Electron flux spectrum in range 200keV to 3MeV can be unfolded from charging currents via response function curves
Total ionizing dose (TID)	Measurements in krad(SiO <sub>2</sub> ) at two shielding depths: 2mm Al plus the 250µm Kovar RadFET lid 5mm Al plus the 250µm Kovar RadFET lid

The lower module houses the ‘generic processor board’ which accommodates the housekeeping elements including power conditioning, microprocessor, analog-to-digital converter, memory, input/output ports and data interfaces. A functional block diagram of CREDANCE is shown in Fig. 2. The outputs from the various sensors are sampled periodically by the internal CREDANCE computer and stored to memory. The default sampling interval is 5 minutes but shorter or longer intervals can be commanded if desired. The stored data is then downloaded to DSX under command from the spacecraft on-board computer.

The overall CREDANCE housing has dimensions 126 x 185 x 60 mm and a total mass of 1.7 kg. CREDANCE is fixed to the exterior of DSX under a thermal blanket to provide exposure to the space radiation environment. A significant contribution to the mass of the unit comes from the thick (5 mm Al) walls used to protect the internal electronics from radiation damage – while such thick walls are not required for the DSX mission, they were essential for the higher radiation Giove-A mission mentioned above.

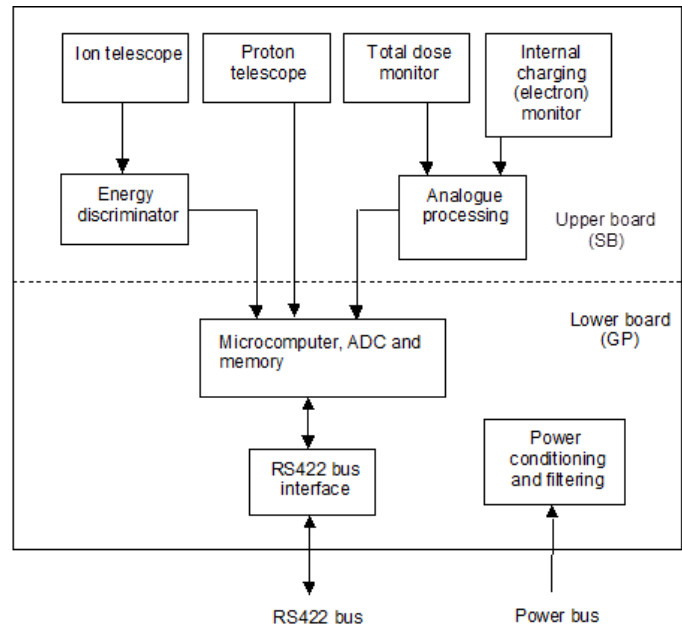


Fig. 2. Block diagram of CREDANCE.

A. Proton Sensor

CREDANCE measures the flux of protons with energy greater than approximately 40 MeV. Lower energy protons are eliminated by the shielding applied around the detector. Two co-axial, 300 µm-thick, fully-depleted silicon diode detectors are arranged in a telescope format as shown in Fig. 3. The detectors are set to trigger upon an energy deposition in the diodes of 500 keV. Protons detected in the upper diode only cause the ‘proton non-coincident’ counter to increment. Protons detected simultaneously in both detectors cause the ‘proton coincident’ counter to increment. The co-incident counter provides a better-defined solid angle of acceptance and thus also a more clearly defined energy threshold. These two proton counters are read out periodically and their contents are placed into memory for later download within the telemetry packet. The accumulation time is the interval between data collection cycles. The counters are reset upon being read out. Both counters are 24 bits long.

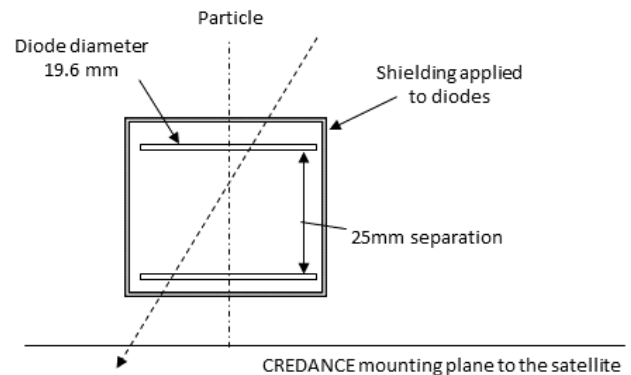


Fig. 3. Diode telescope arrangement.

The telescope axis is perpendicular to the CREDANCE mounting plane and so sees mainly particles from one hemisphere but, depending on spacecraft shielding, it is possible that a small number of very energetic particles from the spacecraft direction may also reach the detector.

### B. Ion LET Sensor

The linear energy transfer (LET) spectrum of ions in space is of critical importance because it plays a key role in determining single event effect rates. The LET of an ion is the energy deposited per unit length as it travels through a material, normalized to unit density: i.e.

$$\text{LET} = 1/\rho \cdot \{dE/dx\} \quad [\text{MeV}/(\text{g}\cdot\text{cm}^{-2})] \quad (1)$$

where  $\rho$  is the material density ( $\text{g}/\text{cm}^3$ )

E is the particle energy transferred to the material (MeV)

x is distance travelled in the material (cm).

CREDANCE measures the ion LET spectrum using a telescope arrangement identical to that illustrated in Fig. 3. However, in this case the amplitude of the signal generated in the upper diode is subjected to pulse-height analysis. Each pulse is categorized into one of 32 bins corresponding to certain LET ranges. The LET range is listed in Table I. Each particle falling within a particular bin increments a counter corresponding to that bin.

There are 32 counters associated with the ‘non-coincidence’ pulse height discriminator which registers counts when a particle is detected in the upper diode only (i.e. no triggering of the lower diode occurs). The number of bits in each counter reduces as channel number increases since the expected number of counts per sampling interval reduces. The final bin is an integral measurement of those ions with LET greater than the threshold. There are a further 32 bins and counters which will increment only when a particle is detected in both the upper diode and the lower diode: these are the ‘ion coincidence’ counters. The lower diode trigger threshold is set to the same LET as the lower threshold of the first ion channel. Again the number of bits in each counter reduces as the channel number increases.

### C. Electrons and Internal Charging

CREDANCE measures internal charging currents in a stack of three circular charge-collector plates (SURF detector): see Fig. 1 and Fig. 4. In front of the stack of plates there is a level of shielding which is equivalent to 0.5 mm Al, including the effect the covering thermal blanket. These thicknesses of the plates and shielding are chosen to be representative of typical dielectric/shielding combinations within many spacecraft where we might wish to know the level of hazard. Each collector plate is connected to an electrometer to measure deposited current. The plate diameter (70 mm) is chosen to ensure that deposited currents are within a measurable range when within the Van Allen belts, but also allowing sufficient headroom to ensure that exceptionally severe environments will not cause saturation. The dominant particle type is indicated by the polarity of the current detected. Any deposited protons will contribute a positive current. From a charging perspective it is

only the net current which is of importance, so SURF always accurately reports the charging threat.

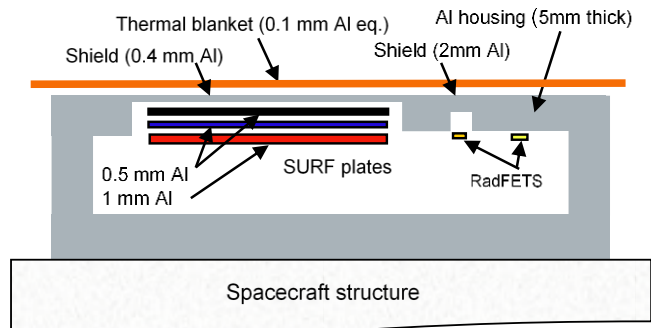


Fig. 4. Configuration of the SURF sensor plates and RadFETS.

Where one species dominates (such as in the outer belt) particle fluxes can be unfolded via the response functions for each plate: 3-D simulations using the MCNPX radiation transport code have been obtained for electrons and these are shown in Fig. 5. A number of unfolding techniques are available as described in Ryden et al. [13], and Sandberg et al. [11]. In the inner belt where protons and electrons are present caution is required as both can contribute to the current.

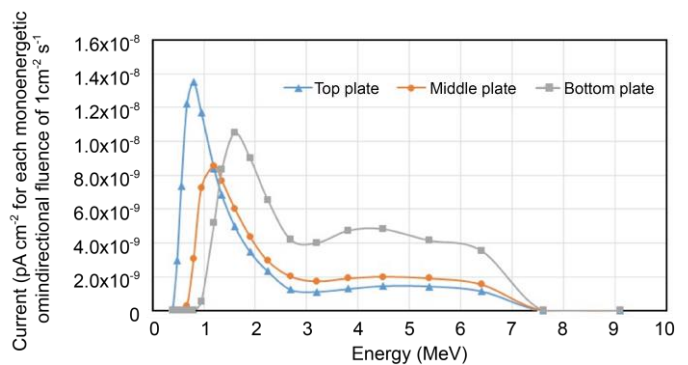


Fig. 5. Response functions for each SURF plate obtained via 3D MCNPX simulation. Note the bottom plate is thicker than the other two.

The SURF sensor was calibrated prior to launch by injecting known currents into the plates and also a number of reference irradiations under a strong Sr-90 source were undertaken in the same way as described for the sister instrument on Giove-A [13]. For each plate there is both a high-sensitivity and low-sensitivity channel in order to provide a wide dynamic range. The low-sensitivity channel produces a (dynamic) output of 10 mV/pA and the high-sensitivity (dynamic) output is 500 mV/pA. Note that analog-to-digital quantization limits resolution to 10 fA in the high sensitivity channels. Certain current levels will be registered in both high and low sensitivity channels (overlap).

For each current measurement channel there is also a certain ‘offset’ (i.e. a reading even if there was no irradiation). This arises due to unavoidable internal standing currents and voltages associated with the amplifier system. In order to monitor any long-term drift in these due for example to aging, temperature changes or total dose, there is a ‘control’ channel. This control amplifier channel is not connected to a collector plate but is otherwise the same as the other amplifier chains.

The reading obtained can be used to implement corrections of drift in offsets although in past missions this has not normally been required as offsets are only of significance in very detailed analysis. When hazard levels are high, currents detected will always be much larger than the offsets. A measurement of the temperature in close vicinity to the SURF amplifiers is available in the housekeeping data.

#### D. Total Ionizing Dose (TID)

Total ionizing dose (TID) in krad(SiO<sub>2</sub>) is monitored by two RadFETs located on the sensors board and positioned just underneath the 5 mm thick lid of CREDANCE (Fig. 1 and Fig. 4). The lid is thinned out to a 2 mm thickness above one RadFET to increase its exposure. As metal-oxide semiconductor (MOS) devices, RadFETs provide a good indication of the TID effects of radiation on CMOS microelectronics in particular. The RadFET is simply a MOS transistor with an especially thick gate oxide to increase radiation sensitivity [14]. The RadFET devices in CREDANCE are procured from Tyndall. The device type is ESAPMOS04, and has a 400 nm gate oxide thickness.

In CREDANCE both primary RadFETS are operated completely unbiased except during the brief read-out periods. This mode of operation minimises fade (annealing). This also means that if the power to CREDANCE is temporarily interrupted it does not affect the accumulation of dose data. The FET itself is located in a ceramic dual in-line (DIL) package with a 250  $\mu$ m Kovar lid (the standard packaging as supplied by Tyndall). Temperature dependence of the RadFET is minimized by operating at a bias current of 12.5 microamps which is the point of zero temperature co-efficient for these devices. Temperature monitoring for each RadFET is nevertheless provided. See Table II for a summary of the TID monitoring.

TABLE II  
RADFET TID MONITORING SUMMARY

	RadFET1	RadFET2
RadFET Tyndall serial no.	256	257
RadFET location	Top RadFET as viewed in Fig. 1 Located immediately under the 5mm Al lid (within CREDANCE housing)	Lower RadFET as viewed in Fig. 1 As for RAD1 but with lid thinned to 2mm Al depth over a diameter of 3mm above device.
Biasing	True zero bias except during readout	True zero bias except during readout
RadFET lid	250 $\mu$ m Kovar	250 $\mu$ m Kovar
Bias constant current (as set)	12.5 $\mu$ A	12.5 $\mu$ A
RadFET temperature monitor	Measured at the RadFET mounting seats	Measured at the RadFET mounting seats

### III. DOSIMETRY INTER-COMPARISON AND MINIATURIZATION EXPERIMENT (DIME)

Spacecraft systems are subject to a variety of different radiation environments depending on their satellite's location in space, their location within the spacecraft, and whether they are in the path of a solar event. Risk of a given radiation effect depends on the orbit and the shielding surrounding the vulnerable system, as well as the solar activity arriving at the satellite. These radiations can generate first, a variety of problems due to the gradual deterioration of circuits due to TID and TNID or second, potentially catastrophic single-event effects (SEE). The latter are typically independent of previous exposure, and so are as likely to induce SEEs at the beginning of the mission as at the end. SEE are typically generated by traversals of a SEE-sensitive volume by a particle that has a high effective LET or by the deposition of a similarly large amount of localized energy through a nuclear spallation reaction. If important systems malfunction, it is important that spacecraft operators quickly determine which of these types of radiation effect has been the most plausible cause of the problem.

The equipment necessary to characterize in detail the particles and their energies that comprise the radiation environment at a given location within a spacecraft are often too bulky and require too much power to fly on any but dedicated research satellites. Moreover, the data collection and analysis from such elaborate measurements would not be completed in time for emergency situations nor would they provide data on the efficacy of different levels of shielding. Simple dosimeters that provide measurements of TID without some effort at energy discrimination or some measurement related to SEE potential will not provide the information required for spacecraft operators to characterize system failures or even increases in sensor noise, especially at locations that have significant amounts of shielding. The purpose of DIME is to provide system designers with simple dosimetry choices that can be easily integrated without significant sacrifice in volume, mass, or power and yet provide useful, practical, and easy to interpret data. We describe in what follows two approaches that were divided onto two 3U boards (DIME 1 and DIME 2) depending on whether they are completely passive or require continuous power during data collection. These approaches utilize inexpensive commercial devices and involve digital electronic readout.

#### A. DIME 1: Passive Board - Power Off Except to Download Data

In this sub-section, and its companion sub-section on DIME-2, we describe a set of simple dosimeter systems that are designed to characterize the environment in terms of the specific radiation effects of concern, in particular: TID, TNID and SEE and to provide data that can be easily interpreted by the spacecraft operator. DIME consists of six dosimeter systems placed on two 3U boards, each board with its own processing capability. It is designed to monitor the varied radiation environments of space in terms of the radiation effects of principal interest. The first board, DIME-1, shown in Fig. 6,

consist of nine dosimeters, six RadFETs under different thicknesses of aluminum and tantalum hemispherical shields, and three unshielded Floating Gate Metal-Oxide-Semiconductor (FGMOS) dosimeter arrays. This board does not require power during radiation exposure. It is only powered up to read the accumulated absorbed dose. The RadFETs provide data on TID under three different levels of aluminum and tantalum shielding. The remaining three devices are Ultraviolet Programmable Read-Only Memories (UVPROMs) consisting of arrays of FGMOS transistors which are suitably programmed to monitor the charge remaining on the floating gates by reading the logic state of each transistor.

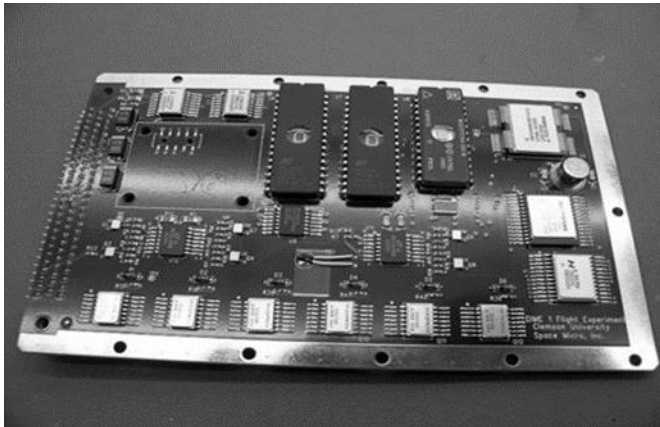


Fig. 6. DIME 1 is shown with six RadFETS along the bottom of the board and three UVPROM dosimeters along the top. The three UVPROMs programmed as dosimeters are identified by windows and lengths, the shorter device is the Intel 27C64. The board has a mass of 0.2 kg and requires < 0.5 W to read the sensors.

The three UVPROMs on DIME 1 are commercially available memory devices that have been programmed as dosimeters following recipes to provide TID measurements over a wider range of exposure levels than is currently available with RadFETs as well as providing some single-event upset measurements as a function of threshold for upset (critical charge) in three non-volatile memories [15-17]. One device is an Intel 64K UVPROM and the other two are ST Micro 8M UVPROMs. The Intel device provides valid data over only the first 50 krad(Si) of absorbed dose, but it provides a simple digital readout (number of bit flips) that is proportional to the TID. The readout is a simple measurement of about 1 rad(Si) per bit-flip. Therefore, a very quick and accurate estimate of the absorbed dose can be immediately obtained by reading the change in the number of bit flips.

### 1) Technical Details of DIME-1

The flight board for DIME-1 is shown in Fig. 6. It is designed to fly in a power-off state while acquiring data. The TID effects being monitored are cumulative, and all reads are non-destructive. The board contains six RadFETS aligned along the bottom of the board. During flight, they sit under hemispherical shields of different thickness of shielding material, three aluminum (Al) and three tantalum (Ta). The three FGMOS dosimeter arrays are aligned at the top of the board.

### 2) TID Measurements with RadFETs

RadFETs are a standard form of dosimeter, and space workers have considerable experience with them [18]. We refer the interested reader to the Tyndall website for more detailed information about the type of P-channel Metal-Oxide-Semiconductor (PMOS) dosimeters used here as well as calibration data. They are from the same lot as those used by NASA for dosimetry elsewhere on SET. Data will be collected at different points along the orbit described in the introduction. Measurements and conversions to TID will be made available for comparison with the relevant ESA and NASA models. These measurements will be valid according to currently available calibration data for about the first 100 krad(Si) of TID where the data fits a model of the change in turn-on voltage,  $\Delta V$ , where D is the absorbed dose in rad(Si):

$$\Delta V = \alpha D^\beta \quad (2)$$

The values of  $\alpha$  and  $\beta$  depend on the production lot, but  $\alpha$  typically ranges from 0.006 to 0.03 with  $\beta$  typically around 0.4 to 0.7.

### 3) TID Measurements in FGMOS Arrays

The FGMOS transistors are distributed in the standard pattern for UVPROM memories. In fact, commercial memories were programmed as dosimeters for flight parts on DIME-1 according to recipes outlined in McNulty et al. [16,17]. Programming consists of dividing the memory array into 32 regions or blocks. All memory cells in a given block are programmed by loading the same amount of charge on every floating gate within a block. The amount of charge on programmed cells increases linearly with the block number starting with the least charge on cells in Block 1 and the most charge stored on gates in the cells of Block 32. All cells in Block 1 should be in the “1” state while all cells in Block 32 should be firmly in the “0” state. Somewhere in between, there is a transition region where the blocks have contributions of both cells in the “0” state and cells in the “1” state. The UVPROMs are read as they normally would be when they are programmed as memories (fully charged for the “0” state and no charge for the “1” state). The total number of cells in the “1” state are counted and included in the telemetry for each block packet.

The active transition region consists of those blocks where the cells are distributed between the two states. This is illustrated in the response curve shown in Fig. 7 where the number of cells in the “1” state is plotted versus the block number that the cells are in. Plots are given for absorbed doses of 10, 110, and 910 rad(Si). The difference in the three plots is restricted to the transition region. The cells in the transition region change states even when exposed to relatively small amounts of radiation ( $\ll 1$  rad(Si)) while more than 1 Mrad(Si) is needed to flip all the cells in the array. The response curves shown in Fig. 7 shift to the right following exposure to ionizing radiation, but the shift is small even for doses as high as 1 krad(Si). The integral under the curve, which is just the total number of cells in the “1” state, is a more sensitive monitor of absorbed dose. Better still is the total number of “0 to 1” transitions induced as a result of exposure to TID, as illustrated in Fig. 8 for the same data set

shown in Fig. 7. The data sets obtained with the M27C64 shown in Fig. 9 for exposure to protons and electrons covers a much larger range of absorbed dose than is expected over the SET mission, and each data point in Fig. 9 was carried out with a different device. This curve gives us confidence that we can calibrate different dosimeters from those chosen for flight [15]. Calibration data for the 27C801 are shown for exposure to protons and electrons in Fig. 10. While there are significant differences between the electron and proton data below 1 krad(Si), these differences anneal away with time.

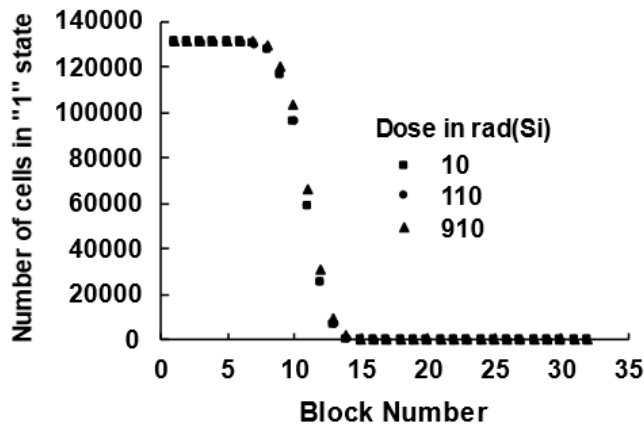


Fig. 7. Response Curve: The active region is the transition region of memory blocks that contain some cells in the “0” state and some in the “1” state. The transition region shifts gradually to the right. Shifts from doses below 1 krad(Si) are clearly difficult to distinguish.

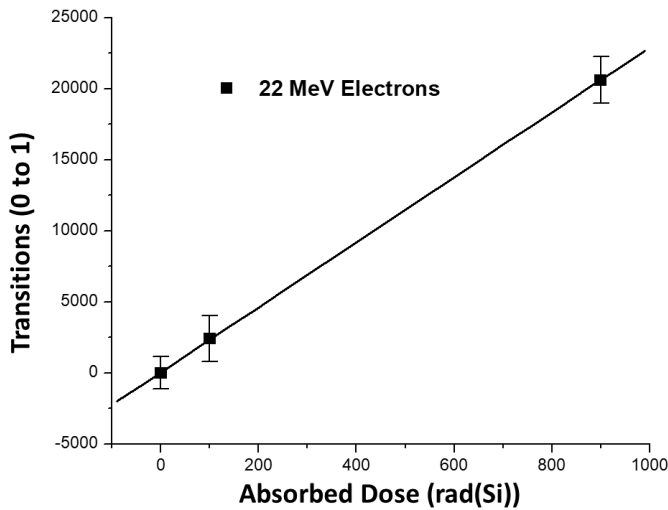


Fig. 8. The number of cells in the “1” state plotted versus the TID exposure measured in rad(Si), for the same three exposures illustrated in Fig. 7. The best-fit curve appears to pass through the origin, shown offset in the figure. The sensitivity for this 27C801 at low doses is roughly 20 flips per rad(Si).

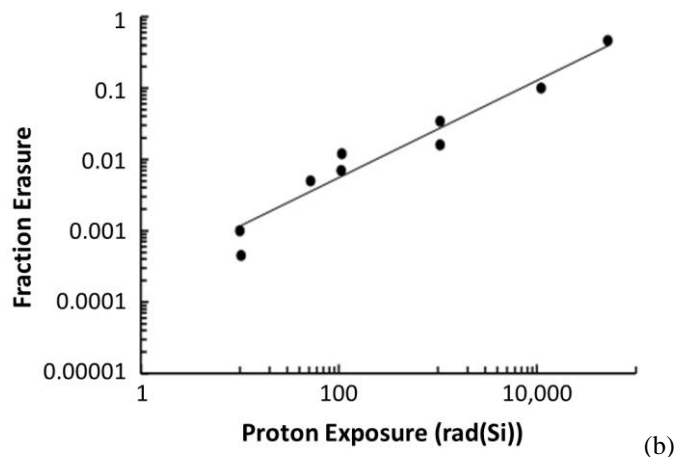
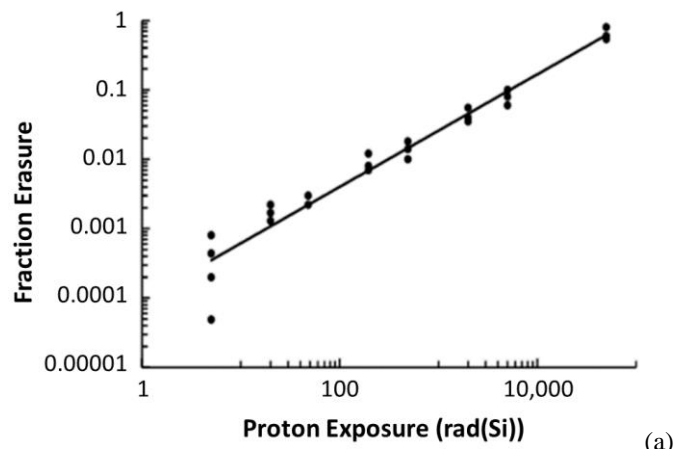


Fig. 9. Number of 0 to 1 flips versus absorbed dose for Intel’s M27C64. The UVPROM is programmed as a dosimeter. Calibration is shown for 48 MeV protons (a) and 6 MeV electrons (b). The number of transitions equals the absorbed dose in rad(Si).

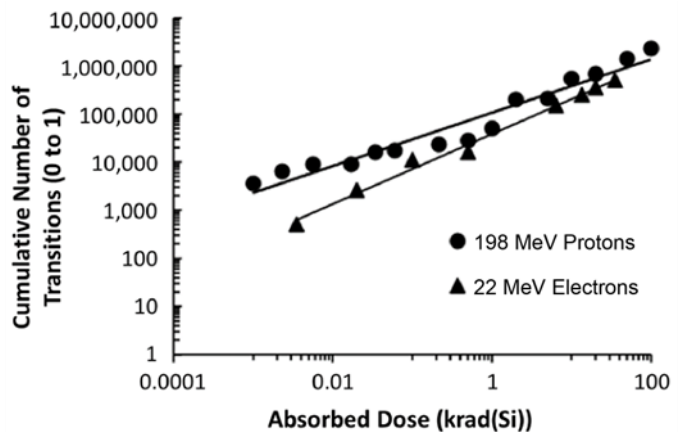


Fig. 10. Number of 0 to 1 flips versus absorbed dose for 198 MeV protons and 22 MeV electrons on the 27C801. There is a significant difference between electrons and protons at low doses but not above 1 krad(Si). This difference anneals over time.

The curves of all devices tested were roughly linear on log-log plots, which suggested they followed power laws. This meant they underwent “0” to “1” transitions,  $\Delta N$ , with absorbed dose,  $D$ , according to

$$\Delta N = \alpha D^\beta \quad (3)$$

Where  $\alpha$  can range from 1 to 20 or more and  $\beta$  ranges from 0.7 to 1.0. The perfect FGMOS device, for dosimetry purposes, has  $\beta = 1$  and  $\alpha$  as large as possible. The M27C64 Intel device has output that fits Eq. (3) with  $\alpha = \beta = 1$  which makes for simple readout since the number of bit flips equals the dose in rad(Si). However, it has less sensitivity and limited range compared to the 27C801. Comparison between the dose–response results for electrons and protons are shown for both devices in Figs. 9 and 10. The 27C801 has greater sensitivity and range but readout requires additional analysis.

#### 4) SEU Measurements in FGMOS Arrays

Cells in blocks to the right and left of the transition region start out with different amounts of charge on their floating gates (proportional to the block number), and as a result, have different thresholds for upset. Cells in the “1” state can flip to the “0” state following an increase in negative charge due to interface states while those originally in the “0” state flip to “1” due to the combination of a removal of negative charge from the floating gate and an increase in negative charge in the form of interface states. Monitoring the number of isolated bit flips beyond the transition region provides counts of SEU events as a function of threshold or critical charge. In the analysis, one must record when an event occurred since the critical charge is changing with block number due to absorbed dose. Estimating the contribution of single events is an important consideration when using the array as a dosimeter because it may affect the measured dose.

#### B. DIME 2: Active Board

On DIME 2 the LET 1&2 instruments receive continuous power for data exposure and readout, while the Optically Stimulated Luminescence (OSL) daughter-board is passive for data collection. All readouts destroy the accumulated data.

A photograph of Board 2 is shown in Fig. 11 with the covers of the LET spectrometers and the OSL removed. Board 2 consists of 3 dosimeters and the complete support electronics needed for the operation and readout of each. Two of them, the LET spectrometers, LET 1, on the left, and LET 2 are located on the bottom of the board as well as the OSL instrument which sits on its daughter board at the lower right. The latter measures TID like the dosimeters on DIME 1 and accumulates data whether power is on or off. The LET devices measure the energy deposited in the sensitive volume and provides an estimate of the distribution of effective LET.

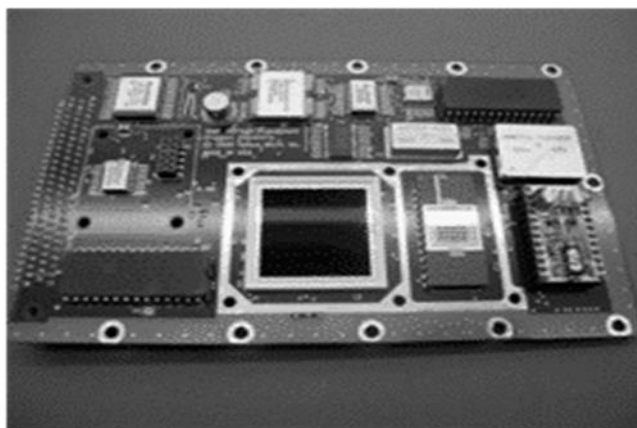


Fig. 11. Photograph of the DIME 2 board with the cover of LET 1 and 2 removed. The OSL dosimeter is on a daughter board at the lower right.

#### 1) Measurement by OSL

A schematic of the circuit laid out on the OSL daughter board is given in Fig. 12. The 300  $\mu\text{m}$  thick layer of OSL material is sandwiched between a 950 nm infra-red emitting Light-Emitting Diode (LED) and a GaAsP photodiode. Ionizing radiation generates electron-hole pairs in the OSL material, a fraction of which are trapped in energy levels which output a green light upon recombination. Read-out consists of stimulating the OSL material with the LED whilst signal is measured by the photodetector. The OSL signal is a pulse and the difference between the peak and the tail measures the absorbed dose. Details of the calibration of the light output as a function of absorbed dose are given in Plattard et al. [19]; Vaille et al. [20,21]; Garcia et al. [22]; Deneau et al. [23].

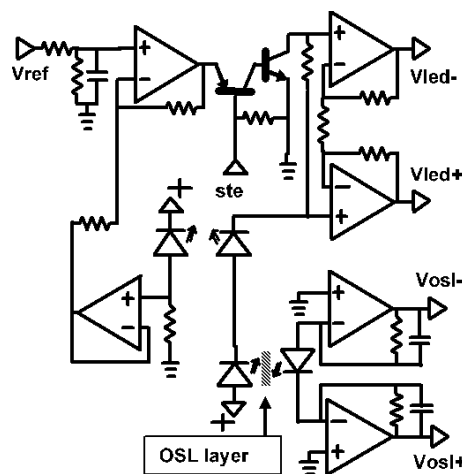


Fig. 12. Schematic of the circuit on the OSL daughter board.

A significant side effect of the exposure of the OSL circuit to intense levels of TID is displacement damage in the LED which causes the light emission by the LED to decrease. A feedback loop monitors the LED and maintains the output power constant. This increase in the current required to maintain the LED output is measured and telemetered. It is used to calculate TNID using a calibration as described in Garcia et al. [22].

### 2) Details of the LET Instruments

The LET instruments are commercial p-i-n diodes supported by circuits required for measurement and telemetry of the energy-deposition spectrum. When exposed to energetic charged particles, a p-i-n diode measures a distribution of pulse heights, each proportional to the energy deposited within the sensitive volume of the detector [17]. If the sensitive volume of the detector is sufficiently large that all the energy from the incident charged particle is collected, the measured energy-deposition spectrum is identical to the incident energy spectrum of the particles. At high incident energies, however, collection of the total incident energy is not practical. Only the energy loss generated in the sensitive volume of the detector by the incident charged particle and the energy loss from the secondary charged particles emerging from any nuclear reactions contribute to the measured pulse-height event. Elastic nuclear reactions and spallation reactions dominate the large energy-deposition events because of the high effective LET and short range of the recoiling nucleus or nuclear fragment. This so-called effective-LET spectrum can be calculated from pulse-height measurements obtained from simple silicon solid-state detectors, photodiodes, or arrays of p-i-n mini-junctions. These detectors are rugged, inexpensive, and lightweight instruments that require little power and provide data in a form suitable for comparison with the environmental models which are combined with available interaction models such as CUPID [24]. Energy spectra are superior to LET spectra for studying the space environment and managing radiation effects, but for high-energy protons, the practicality of either collecting all the incident particle's energy or developing an accurate time-of-flight system precludes flux measurements at high energies in small efficient instruments.

### 3) Potential Analysis of LET Spectra

A previous paper [25] determined the relative contributions from the elastic-scattering events, pion-production events, and direct-hits by cosmic rays and grazing low-energy protons from the pulse-height spectrum measured with a simple silicon optical detector, the UV100. The method was first demonstrated on data obtained from the Pulse Height Analyzer (PHA) instrument flown as part of the Microelectronics Package Experiment on the Combined Release and Radiation Effects Satellite (CRRES). In recent years, a simple algorithm for obtaining the primary particle energy spectrum from pulse-height measurements generated by thick solid-state detectors has been developed and shown to provide good agreement with established models of the energy spectrum of the Los Alamos National Laboratory neutron source. A full description of the methodology is given in Kinnison et al. [26]. Since protons and neutrons undergo similar interactions at high energies, the technique should also be applicable to thin detectors in high-energy proton environments provided that the response of the detector to mono-energetic protons can be determined by experiment or modeling. This response-function method can be used to determine the incident-energy spectrum of high-energy protons trapped in the Earth's inner radiation belt from the data measured with small photodiodes, a single p-i-n diode in the

case of LET 1 and an array of p-i-n diodes wired in parallel in the case of LET 2. The circuit of LET 1 was constructed with rad-hard components while LET 2 is supported by a commercial pulse-height-analyzer circuit which, while designed for use in low-earth orbits, was designed before the availability of modern rad-hard components. Both LET 1 and LET 2 were calibrated by exposures to protons accelerated to various energies at the Indiana University and University of California at Davis Cyclotrons. Examples are shown in Figs. 13 and 14.

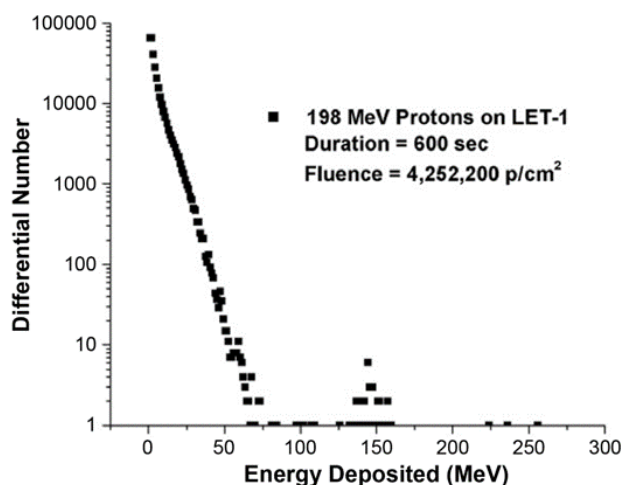


Fig. 13. Differential number of events versus energy deposited in the event measured in LET-1.

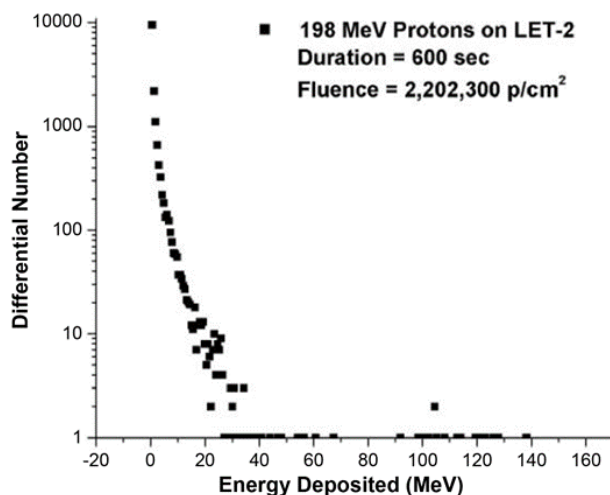


Fig. 14. Calibration of the LET-2 spectrometer exposed to 198 MeV protons at the Indiana University cyclotron.

The original CUPID simulation codes were shown to give reasonably good agreement with the experimental data, especially for incident energies below 200 MeV and large-energy-deposition events, the type that initiate SEE. Above 200 MeV incident energy, pion production begins to impact the large-energy-deposition events and CUPID had to be modified to include pion production. The fraction of events resulting in pion production, according to simulations, is plotted versus the energy that would have been deposited in the absence of pion production in Fig. 15. Clearly, the total fraction of pion events is small, but their impact on high energy-deposition events is

very large, as can be seen from Fig. 16. It is important to note that the practical result of producing a pion is to remove 140 MeV from the predicted energy deposition in small volumes. Either the pion produced has no charge or, if charged, is minimum ionizing, and in either case it deposits very little energy before exiting the sensitive volume. This reduces the large-energy-deposition events from predictions that do not take pion production into account and increases the number of low-energy events by the same amount.

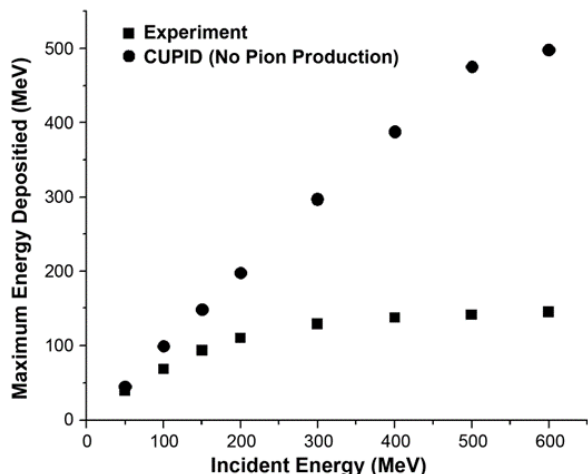


Fig. 15. Maximum energy deposition measured in a Si solid-state detector with a cylindrical volume of  $2 \text{ cm}^2 \times 0.5 \text{ cm}$  versus the energy of the incident neutron. The increasing difference between experiment and the original version of CUPID is that that version did not include particle production ( $\pi^-$ ,  $\pi^0$ ,  $\pi^+$ ). A neutral pion removes 140 MeV from the energy deposition while a charged pion also removes 140 MeV since it generates minimal energy within the sensitive volume.

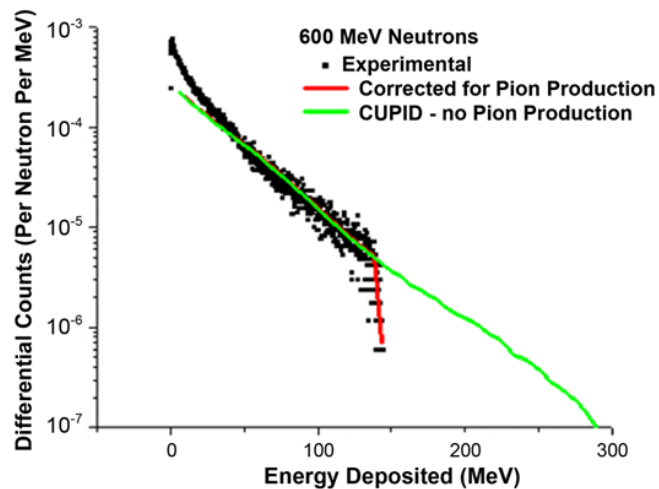


Fig. 16. Differential event cross section versus the energy deposited in an Ortec Si Li-drifted detector. Comparison is made with CUPID simulations with and without pion production. The significant difference between theory and experiment at low energy depositions is due to elastic scattering events.

CUPID simulations [24] were then carried out for the UV100 photodetector used in the CRRES PHA experiment [25] for protons incident at 24 different energies in intervals of 10 MeV from 30 to 90 MeV and in intervals of 30 MeV from 90 to 600 MeV. The dimensions of the cylindrical sensitive volume of the photodetector were  $5 \text{ mm}^2$  in cross-sectional area and  $26 \mu\text{m}$  in thickness. Since the probability of an elastic scattering event

depends on the cumulative proton track length in the sensitive volume, the total elastic-scattering-event cross sections were scaled for the UV100 from the values obtained for the Ortec detector [26] by the ratio of the volumes. The energy-deposition in elastic scattering was obtained from the energy transferred to the silicon nucleus. Since the elastic recoils are so short compared to the dimensions of the photodetector, they were assumed to lose all their energy within the detector. The number of events with energy deposition  $ED_j$  to be expected in space can be obtained from the sum over the product of the fluence of protons with incident energy  $E_i$ ,  $F(E_i)$ , and the cross section  $\sigma_i(ED_j)$  that a proton with energy  $E_i$  has for depositing energy  $ED_j$ .

$$N(ED_j) = \sum_i F(E_i) \sigma_i(ED_j) \quad (4)$$

where  $E_i$  represents each of the 24 incident energies for which the combined CUPID and elastic scattering cross sections  $\sigma_i(ED_j)$  for depositing energy  $ED_j$  have been calculated. Eq. 4 can be inverted to obtain the fluence as a function of energy for the incident trapped protons. The experimental CRRES PHA data for orbits 4 through 584 were substituted for each value of  $N(ED_j)$  in Eq. 4 and the equation was best fitted to find the optimum values of the fluence  $F(E_i)$ . The values of the fluence obtained are plotted as black squares as a function of  $E_i$  in Fig. 17 and compared to the predictions of the NASA models. The agreement is reasonable above 100 MeV.

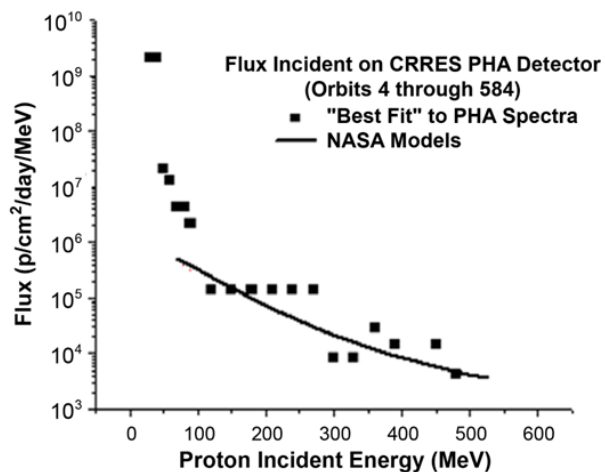


Fig. 17. Comparison of the average “best fit” flux of protons incident on the CRRES PHA experiment during orbits 4 through 584. The squares are the results of the best fit to the PHA measurements. The solid curve represents the predictions of AP8 using the USAF B-L coordinates. The agreement is excellent at high incident energies and reasonable between 50 and 100 MeV. The two lowest data points (30 and 40 MeV) are not in agreement with the model. However, these two data points are dominated by energy depositions between 13 and 20 MeV. Energy depositions above 13 MeV can be generated by protons entering the detector at grazing angles with incident energies between 20 and 25 MeV. A reasonable flux of 20 – 25 MeV protons for the CRRES environment would be sufficient to generate these two data points.

#### IV. THE ENHANCED LOW DOSE RATE SENSITIVITY (ELDRS) EXPERIMENT

Satellites and other space-based systems are vulnerable to the harmful effects of space radiation. Ionizing particles, particularly protons and electrons, either emitted from solar

flares, cosmic rays, or trapped in the Earth's magnetosphere can have a significant impact on the operation of space electronics. Solar and trapped particles are a significant threat to a specific class of electronic components, bipolar devices and circuits. These parts are used ubiquitously in spacecraft systems to perform voltage amplification and other primarily analog functions. The exposure of bipolar components to ionizing radiation from protons and electrons is a great concern for a variety of reasons: 1) the particles typically have high energies and are not easily stopped by spacecraft shielding, 2) charged particles, particularly protons, are responsible for both ionization and displacement effects, and 3) many bipolar parts exhibit Enhanced-Low-Dose-Rate-Sensitivity (ELDRS). ELDRS is characterized by the enhancement in degradation when parts are exposed to radiation at low dose rates, characteristic of the space environment. ELDRS phenomena pose significant problems for the qualification of bipolar parts for use in proton and/or electron rich, low-dose-rate environments.

An understanding of low-dose-rate effects is essential to the mission of the LWS SET, i.e., "to accommodate or mitigate effects of solar variability on spacecraft design and operations." The ELDRS experiment is assembled on a small circuit board, approximately 10 cm x 16 cm (Fig. 18). It performs real time measurements of ionizing-radiation-induced degradation in bipolar junction transistors (BJTs) in the low-dose-rate space environment. The board measures parametric degradation, specifically changes in current on COTS BJTs integrated onto silicon die, manufactured in Texas Instrument's (formerly National Semiconductor's) linear bipolar process. Transistor layouts on the die are derived from standard designs used in the TI process.

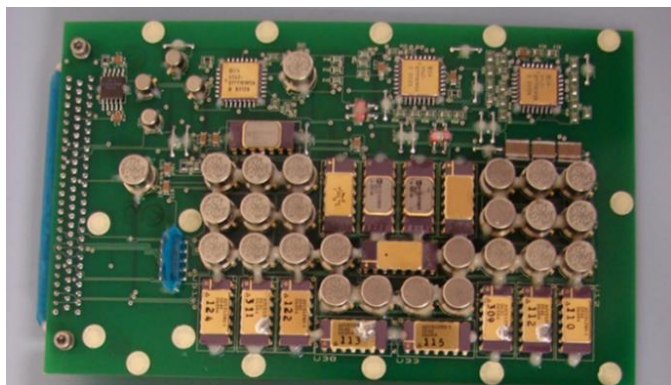


Fig. 18. Enhanced Low Dose Rate Sensitivity (ELDRS) experiment board.

The eight die used on the experiment were manufactured with different protective passivation layers, either phosphorus glass (p-glass) or silicon carbide (SiC). Each die contains three lateral PNP (LPNP) BJTs. One transistor on a die is gated with a thick oxide, another is gated with a thin oxide, and the third is not gated with a thick oxide. The amount of TID damage to a semiconductor device is typically a function of oxide thickness as described in [27], so testing parts with different thicknesses is important for characterizing radiation effects and validating ELDRS models. The un-gated device is a standard LPNP BJT. It uses the same  $p^+$  diffusion and metal mask patterns as most

LPNPs designed in the TI linear bipolar process. The two gated lateral PNP (GLPNP) BJTs are essentially identical to the LPNP except for the inclusion of an independent metal pattern above the active base region, which acts as a gate electrode. A representational cross-section of the GLPNP BJT is provided in Fig. 19, which illustrates the  $p^+$  regions forming the emitter and collector diffused into an n-epi base and a gate terminal deposited on the oxide (thick or thin) above the active base region. Fig. 20 shows the layout of the two GLPNP BJTs. While seldom used in conventional bipolar circuit designs, an independent gate terminal is often included in process monitors and has been shown to be an effective tool for analyzing the effects of TID and TNID [28]. Measurements on gated transistors can be used to separate ionization from displacement effects, which is important for a proton rich space environment [28].

The die were inserted into 14-pin ceramic dual inline packages (labeled 110, 112, 113, 115, 122, 124, 309, and 311 on Fig. 18). Post-packaging modifications were performed on four of the parts to remove in-package hydrogen. The presence of moderate amounts ( $> 0.1\%$ ) of hydrogen gas in a sealed package can cause significantly more degradation to bipolar parts that are exposed to ionizing radiation [29]. The remaining four unmodified parts are estimated to have at least 1% hydrogen inside the package. Thus, we anticipate not only observing an enhancement in BJT degradation as a result of the low space dose rate, but also a distinct difference between the four unmodified, high hydrogen content packages and the modified parts with reduced hydrogen content. We are also assessing the impact of the passivation layer in controlling hydrogen diffusion into the die.

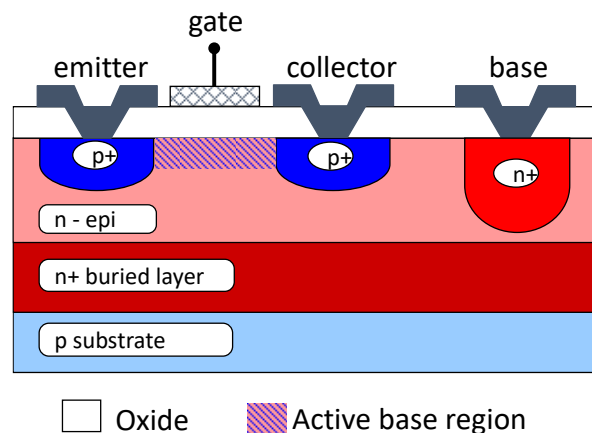


Fig. 19. Representational cross section of GLPNP BJT showing gate terminal deposited over the active base region.

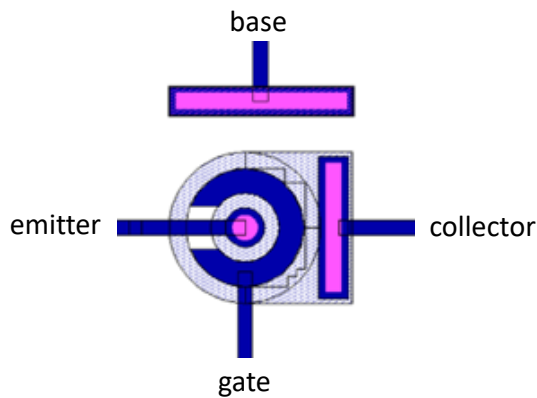


Fig. 20. Layout of gated BJT design on the ELDRS experiment's eight die.

The primary data set collected from the experiments is the BJT base current ( $I_b$ ) vs. base-emitter voltage ( $V_{be}$ ) on the 24 BJTs. Exposure to protons and electrons in space will cause  $I_b$  to increase, reducing the critical parameter of current gain in the BJT. These effects can be observed in Fig. 21, which plots base current on similar part types after ground based, low-dose-rate (10 mrad(Si)/s) irradiations to 10 krad(Si) and 50 krad(Si). Fig. 22 is a plot of initial base current inflight measurements. These data were taken on a p-glass modified (DUT 6), gated BJT with a thick oxide. The curves, obtained 41, 60 and 145 days after launch show the expected increase in base current over time. Since the dose is still low at this point, the data do not show a large change but the monotonic increase over time is an indication that the experiment is working as expected.

Fig. 23 plots the increase in base current ( $\Delta I_b$ ) at  $V_{eb} = 0.5V$  as a function of TID for published ground-based data [29-33]. All data were taken on LPNP devices fabricated on the same TI wafer lot as the parts flown on the LWS SET mission [30]. The results in Fig. 23 include data taken at low dose rate (<30 mrad[Si]/s), elevated temperature (5 rad[Si]/s + 100° C), and high dose rate ( $\geq 39$  rad[Si]/s). The results of the ELDRS experiment will be compared to these data to assess whether low dose rate data, obtained in space, match TID tests performed in laboratories.

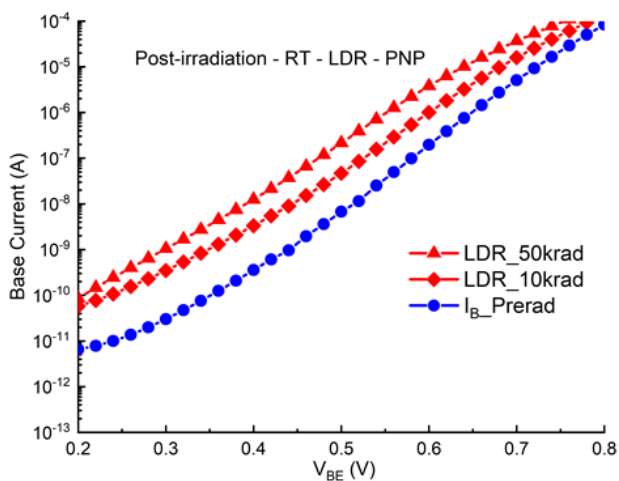


Fig. 21. Pre- and post-irradiation base currents for PNP BJTs as a function of base-emitter voltage,  $V_{be}$ . Irradiation was performed with a ground-based source at a low dose rate of 10 mrad[Si]/s and at room temperature.

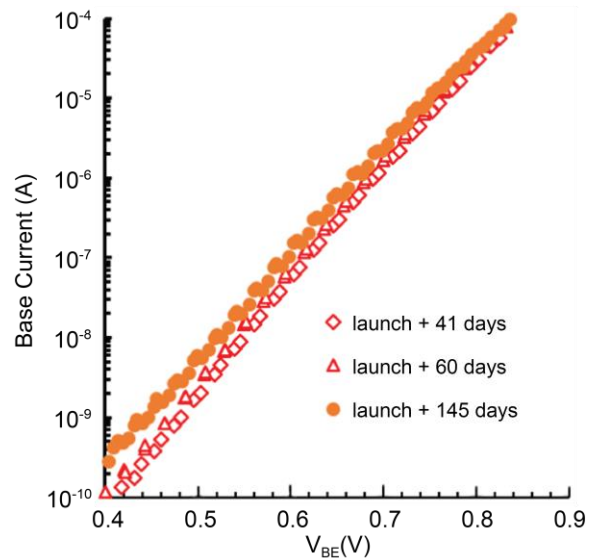


Fig. 22. Initial look at base current inflight data from p-glass modified (DUT 6), gated BJT with thick oxide. The data 41, 60 and 145 days after launch show an expected increase in base current over time.

Key features of the ELDRS board are its design simplicity and, aside from the eight devices under test (DUTs), the radiation hardness of its components. It uses inherently rad-hard mechanical relays (round, canned packages shown on Fig. 18) with hardened basic digital gates (inverters, nands, and nors) to multiplex though the 192 measurement sweeps. Radiation tolerant analog circuits respond to a single off-board digital-enable signal to initiate each test sequence, omitting the need for an on-board controller. A unique log-amplifier design supports a wide range of currents (10 pA to 1 mA) to be measured as voltages between zero and five volts. These analog output voltages, logarithmically scaled to BJT currents, along with the analog input voltage ramp are sampled by the off-board DSX central computer every second until all 24 BJTs are measured. The system turns itself off automatically when the 192 measurement sweeps are completed.

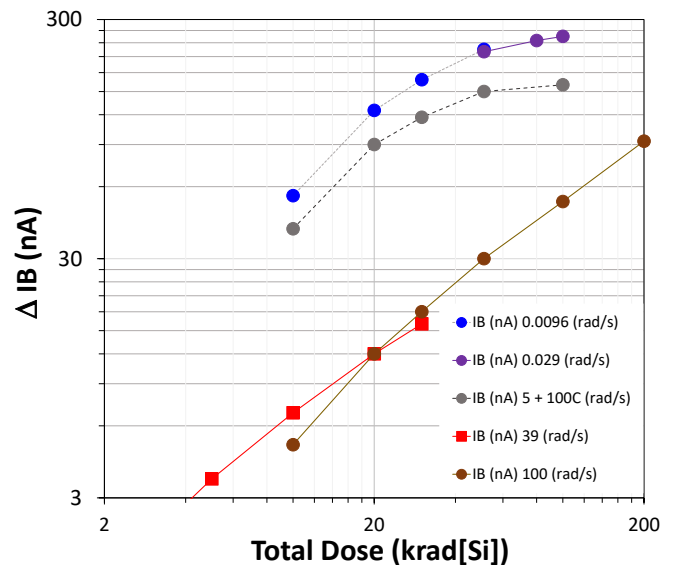


Fig. 23.  $\Delta I_b$  vs. TID for published ground-based data irradiated at various dose rates and temperatures [29-33].

The data acquired from these experiments and subsequent analysis is critical to validating existing models for ELDRS, ionizing and displacement damage effects in BJTs. If successful, the ELDRS experiment will provide, for the first time, direct measurements of space radiation effects on BJTs from a bipolar linear circuit process. The results of this experiment will also support the establishment of reliable ELDRS test standards for bipolar parts used in space applications. Such standards help satisfy the LWS SET program goal of “reducing the requirements for margins to account for uncertainties in the definition of the induced environment and its effects on spacecraft design and operations.” Lastly, this effort will facilitate the development of techniques for mitigating the damaging effects of solar and trapped particles in earth-orbiting and space exploration systems.

## V. THE COMMERCIAL OFF-THE-SHELF-2 (COTS-2) EXPERIMENT

COTS-2 experiment goals are to assess the harsh radiation effects of a medium-earth orbit (MEO) on the reliability of a digital system implemented in a typical Commercial Off-The-Shelf (COTS) device. The case-study digital system (set of crypto-processors) has been designed in a COTS Field Programmable Gate Array (FPGA) based on Static Random Access Memory (SRAM) cells. Furthermore, the digital system has been triplicated to make the design robust and detect the occurrence of failures induced by SEUs in the SRAM cells. The COTS-2 experiment will provide data that will be correlated with previous experimental results issued from fault-injection campaigns and heavy-ion radiation tests carried out at ground level to predict the SEU rate of the designed digital system in the COTS SRAM-based FPGA. The next sections describe and discuss respectively the test platform, the case-study digital system, the test method, and the next steps of the COTS-2 experiment for correlating results obtained at MEO, ground radiation tests, and fault injections.

### A. Test Platform

The test platform of the COTS-2 experiment is a board (Fig. 24) composed of a COTS FPGA and 7 radiation-hardened devices for reliably controlling and monitoring the experiment. The COTS-2 experiment board was built to exclusively observe if the traditional Triple Modular Redundancy (TMR) technique implemented in a case-study digital system on a COTS FPGA can fail in MEO spaceflight as previous works have observed in ground level tests [34-40] as well as in Low Earth Orbit (LEO) [41,42]. The COTS-2 experiment was therefore focused on observing SEU effects only. Note that all devices around the COTS FPGA are protected against radiation effects but they may still fail in spaceflight. The initial goal was to minimize radiation effects in such devices to allow further observing SEU effects in the TMR implemented in the COTS FPGA:

- a) Non radiation-hardened COTS FPGA (Xilinx Virtex-II XC2V1000) that is where a case-study digital system is configured;

- b) Read-Only Memory (ROM) programmed with the FPGA bitstream that represents the case-study digital system;
- c) Processor (LEON2) that executes a program for automatically:
  - a. Configuring the case-study digital system;
  - b. Getting output results of the case-study digital system;
  - c. Reading back the FPGA bitstream;
  - d. Checking for SEUs and failures; and
  - e. Answering commands (processed via interruptions) sent by the central processor of the satellite.
- d) Program memory (ROM) that stores the program executed by the processor;
- e) Data memory (RAM) that stores results of the program executed by the processor;
- f) RS-422 interface for communication with the central processor of the satellite in which the SET payload is embedded;
- g) Thermistor and dosimeter for measuring respectively the temperature and the dose of external ionizing radiation;
- h) Voltage converter for providing suitable operating voltages to the devices.

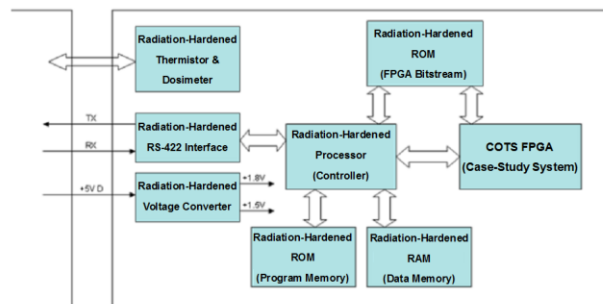


Fig. 24. Abstraction of the COTS-2 experiment board.

### B. Case-study Digital System

The core of the case-study digital system implemented in the COTS FPGA is a commonly used crypto-processor [34], which is based on the Triple Data Encryption Standard (DES3) Algorithm, also called TDEA [35]. The classical DES algorithm encrypts 64-bit data using a 56-bit key in 16 clock cycles whereas DES3 encryption is achieved by three consecutive DES encryptions, requiring thus three 56-bit keys and 48 clock cycles.

The case-study digital system is composed of three chains of 8 DES3 crypto-processors operating for performing 4 encryptions and 4 decryptions. Actually, using the traditional Triple Modular Redundancy (TMR) technique, a chain of 8 DES3 crypto-processors is triplicated and a voter checks the outputs of the three chains as a way to make the case-study digital system robust and detect the occurrence of failures induced by SEUs in one or three of the chains. Fig. 25 illustrates an abstraction of the case-study digital system configured in the COTS FPGA.

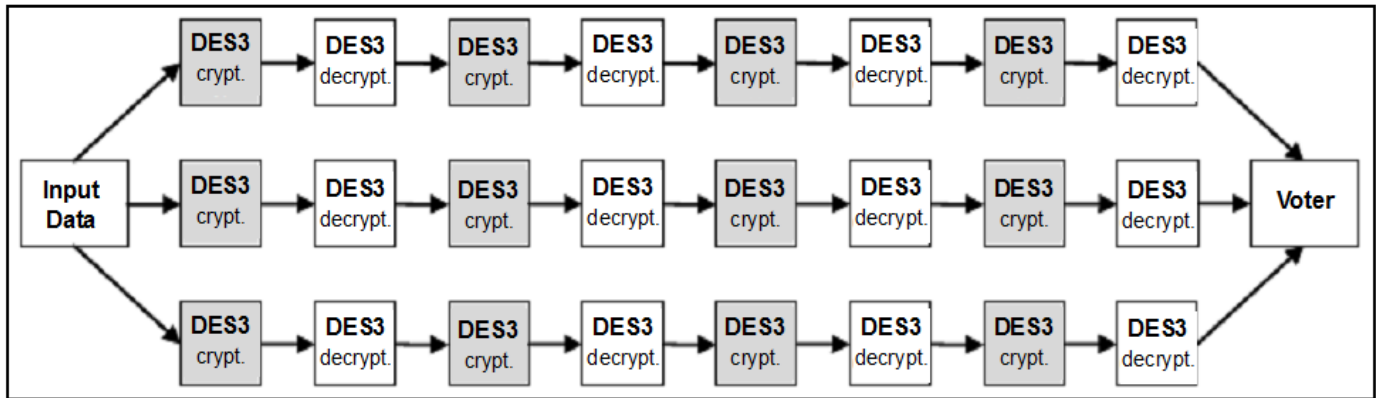


Fig. 25. Abstraction of the case-study digital system implemented in the COTS-2 experiment.

The voter output therefore reproduces a result that is found at the outputs of two or three chains of 8 DES3 cryptoprocessors. Furthermore, according to the results of the chains, an additional 3-bit register is used for storing in which chain (or chains) eventual errors have happened. The possible values stored in this 3-bit register are:

- 000 if the three chains provide the same results;
- 001 if the first chain provides a different result regarding the other chains;
- 010 if the second chain provides a different result regarding the other chains;
- 011 if the third chain provides a different result regarding the other chains;
- 100 if the three chains provide different results;
- 101, 110, or 111 are not used, hence they should not happen in error-free conditions.

### C. Test Method

In this experiment, an **error** is defined as a bit flip in a memory cell of the case-study system. Furthermore, a **failure** is the manifestation of a wrong result at the primary outputs of the case-study system, i.e. the voter outputs provide a value that is not correct according to the expected function of the case-study system.

The test method (Fig. 26) for automatically detecting and reporting the errors and failures induced by SEUs in the case-study system is a program stored in the program memory and executed by the processor, both radiation-hardened devices as Fig. 24 illustrates.

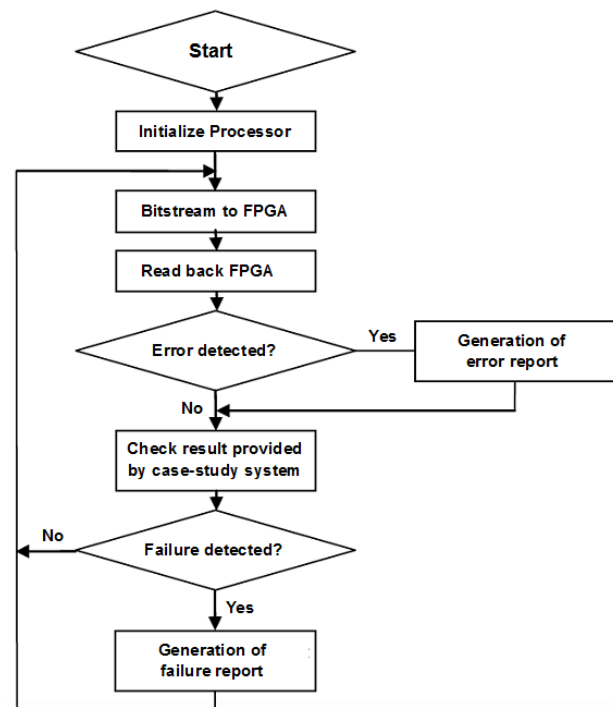


Fig. 26. Test method for automatically reporting SEU-induced errors and failures.

The program regularly reads the FPGA bitstream back and compares it with the error-free bitstream stored in the radiation-hardened ROM. In addition, the program also regularly checks every result provided by the voter outputs, in order to detect potential failures, by using the error-free case-study system result, which is stored in the radiation-hardened memory program. Then, combined with the content of the 3-bit register (defined in section 5.2), we are able to distinguish the following probable situations of errors and failures based on the previously mentioned four testing supports (radiation-hardened devices, bitstream comparison, checker of TMR voter outputs, and logic indicator stored in the 3-bit register):

### 1) *Detected Errors but No Failure*

- a) Bitstream with error(s), 3-bit register indicates error(s), TMR works properly: existence of error(s) in one chain of the case-study system (cases “b”, “c”, or “d” described in section V.B), however the TMR technique is effective as the voter outputs provide an error-free result. The case-study system, therefore, does not result in a failure;
- b) Bitstream with error(s), 3-bit register indicates error(s), TMR works properly: existence of error(s) in the logic indicator stored in the 3-bit register (case “f” described in section V.B), however the TMR technique functions well because the voter outputs provide an error-free result (no failure);
- c) Bitstream with error(s), 3-bit register indicates error(s), TMR fails: existence of error(s) in the chains of the case-study system (case “e” described in section V.B), however the TMR technique does not work properly because the voter is not able to elect with three different results coming from the three chains but the case-study system provides anyway, and by coincidence, an error-free result (no failure);
- d) Bitstream with error(s), 3-bit register indicates no error(s), TMR works properly: existence of error(s) in the FPGA memory cells but no error(s) in the chains of the case-study system (case “a” described in section V.B). The TMR technique is effective as the voter outputs provide an error-free result (failure);
- e) Bitstream with no error(s), 3-bit register indicates error(s), TMR works properly: three hypotheses are more likely:
  - i. The procedure of reading the FPGA bitstream back (and comparing it) failed, and thus the same explanations described in the situations “a” or “b” are applicable;
  - ii. The hardened-radiation processor (controller) failed in computing the 3-bit register;
  - iii. The procedure of comparing the voter outputs with the error-free case-study system results, which are stored in the radiation-hardened program memory, failed;
- f) Bitstream with no error(s), 3-bit register indicates error(s), TMR fails: the same three hypotheses in situation “e” are more likely, however in case of hypothesis “i”, the same explanations described in the situation “c” are applicable;

### 2) *Detected Errors and Failure*

- a) Bitstream with error(s), 3-bit register indicates error(s), TMR fails: existence of error(s) in one chain of the case-study system (cases “b”, “c”, or “d” described in section V.B). Furthermore, the TMR technique fails because the voter outputs provide a wrong result. The case-study system, therefore, result in a failure;
- b) Bitstream with error(s), 3-bit register indicates error(s), TMR fails: existence of error(s) in the logic indicator stored in the 3-bit register (case “f” described in section V.B). In addition, the TMR technique does

not function correctly because the voter outputs provide a wrong result (failure);

- c) Bitstream with error(s), 3-bit register indicates error(s), TMR fails: existence of error(s) in the chains of the case-study system (case “e” described in section V.B). The TMR technique does not work properly because the voter is not able to elect with three different results coming from the three chains, hence the case-study system provides a wrong result (failure);
- d) Bitstream with error(s), 3-bit register indicates no error(s), TMR fails: existence of error(s) in the FPGA memory cells. Although the 3-bit register does not indicate any error in the chains of the case-study system (case “a” described in section V.B), the voter outputs provide a wrong result (failure), then the TMR technique fails, probably because the registers of the voter outputs were directly affected by SEUs;
- e) Bitstream with no error(s), 3-bit register indicates error(s), TMR fails: probably the procedure of reading the FPGA bitstream back (and comparing it) failed, and thus the same explanations described in the situation “a”, “b”, or “c” are applicable;

### 3) *No Detected Errors but Failure*

The bitstream has no error(s), the 3-bit register indicates no error(s) (case “a” described in section V.B), and TMR fails. This situation is probably because another radiation-sensitive resource of the FPGA (e.g. JTAG controller, clock tree, memory element) was upset. Furthermore, this may also be due to the procedure of comparing the voter outputs with the error-free case-study system results (which are stored in the radiation-hardened program memory), and thus the case-study system may not have suffered a failure. Actually the error(s) may be in the processor or program memory.

### 4) *No Detected Errors and No Failure*

The bitstream has no error(s), the 3-bit register indicates no error(s) (case “a” described in section V.B), and TMR works properly with the voter outputs providing error-free results (no failure).

### D. *Correlating Results Obtained at MEO, Ground Radiation Tests, and Fault Injections*

Fault injection campaigns and radiation tests have already been performed in the case-study digital system of the COTS-2 experiment, results and analysis correlating both are widely discussed in Velazco [34].

In the fault-injection campaigns, 426217 faults (emulating errors according to the definition of section 5.3) were randomly injected, and the case-study system was able to tolerate the large majority (96.45 %). By using the 3-bit register mechanism discussed in previous sections, 3.48 % of the injected errors were detected and resulted in no failures due to TMR use. Otherwise, only 0.07 % of the injected errors were not detected and resulted in failures.

The radiation tests were performed at a heavy ion facility, where the case-study system was exposed to two particle species, carbon and argon. The total number of errors observed was 1367, and only 35 of them resulted in failures. Although

the number of failures is small, these results show that the traditional TMR technique may fail, which can be critical depending on the application.

The analysis in Velazco [34] still correlates results from both experiments by using the static cross-section calculated from the data also obtained in the radiation tests, demonstrating error-rate predictions calibrated with fault-injection results and the static cross-section are close to the error-rate results exclusively extracted from the radiation tests. The difference between the error rates is probably due to multiple bit upsets that were not considered in the fault injection campaigns. Furthermore, another reason could be the existence of resources sensitive to SEUs that are not accessible by reading the FPGA bitstream back (e.g., the JTAG controller and the clock tree).

The next step of this work will be correlating such results obtained in fault-injection campaigns and radiation tests with the data obtained at MEO with the COTS-2 experiment in the SET payload. Note that the target COTS FPGA was assessed only through heavy-ion radiation tests. However MEO radiation effects are from both heavy ions and protons. On the other hand, the static cross-section curve for heavy-ion-induced SEUs will allow an estimate of the total number of static SEUs induced by protons with the help of the SPENVIS [43] and PROFIT model [44] tools. First results for the COTS-2 experiment are presented in [45].

## VI. SUMMARY

The NASA LWS SET payload has been reviewed. This included its objectives, experiments and methods, and data taken both in the laboratory and by previous generation space experiments. Given the success of the DSX mission it is expected these payload measurements will help improve the performance of hardware in the space radiation environment by providing additional data on the environment and by improving our understanding of radiation interactions with electronic devices and systems. Environmental data include proton and heavy ion flux, internal charging currents, and total ionizing and non-ionizing dose. Radiation effects include results for ELDRS and for SEE in a commercial FPGA.

## ACKNOWLEDGMENT

The authors thank LWS SET Program Executive at NASA Headquarters, Alan Zide, for guidance. They also acknowledge Jim Ritter of the Naval Research Laboratory for the original suggestion of implementing SET. The authors gratefully acknowledge the dedicated management and engineering teams at Goddard Space Flight Center and the Air Force Research Laboratory that made SET possible.

## REFERENCES

- [1] J.L. Barth, K. LaBel, D. Brewer, G. Withbroe and W. Kauffman, "The Living With a Star program: NASA's role in assuring performance in space and atmospheric environments," *AIAA Proc.*, AIAA-2001-0235, Jan. 2001.
- [2] M.A. Xapsos, "A brief history of space climatology: from the big bang to the present," *IEEE Trans. Nucl. Sci.*, vol. 66, no. 1, pp. 17-37, Jan. 2019.
- [3] Y. Zheng, et al., "Space radiation and plasma effects on satellites and aviation: quantities and metrics for tracking performance of space weather environment models," *Space Weather*, vol. 17, issue 10, pp. 1384-1403, Oct. 2019.
- [4] NASA Research Announcement NRA 02-OSS-04, May 2003
- [5] K.A. Ryden, C. S. Dyer, P. A. Morris, R. A. Haine and S. Jason, "The Merlin space weather monitor and its planned flight on the Galileo System Testbed Satellite (GSTB-V2/A)," IAC paper IAC-04-IAA.4.9.3/U.6.04, *Proc. IEC Congress*, Vancouver, Canada, Oct. 2005.
- [6] K.A. Ryden, A.D.P. Hands, C.I. Underwood and D.J. Rodgers, "Internal charging measurements in Medium Earth Orbit using the SURF sensor: 2005–2014," *IEEE Trans. Plasma Sci.*, vol. 43, no. 9, pp. 3014-3020, April 2015.
- [7] C.S. Dyer, A. J. Sims, J. Farren, J. Stephen and C. Underwood, "Comparative measurements of single event upset and total dose environments using the CREAM instruments," *IEEE Trans. Nucl. Sci.*, vol. 39, no. 3, pp. 413-417, June 1992.
- [8] C.S. Dyer, K. Hunter, S. Lucas and A. Campbell, "Observation of the solar particle events of October and November 2003 from CREDO and MPTB," *IEEE Trans. Nucl. Sci.*, vol. 51, pp. 3388-3393, Dec. 2004.
- [9] K.A. Ryden, H. S. Jolly, A. D. Frydland and P. A. Morris, "A compact electrostatic charging monitor for spacecraft," *1999 Proc. Radiation and Its Effects on Components and Systems*, Abbaye-de-Fontevraud, Loire, France, pp. 120-125, Sept. 1999.
- [10] K.A. Ryden, P. A. Morris, A. D. Frydland, H. S. Jolly, D. J. Rodgers and C. S. Dyer, "Profiles of inner- and outer-belt internal charging currents against geomagnetic parameter 'L': results from the first SURF experiment," *Proc. 7th Spacecraft Charging Technology Conference*, Noordwijk, The Netherlands, ESA-SP476, pp. 341-344, April 2001.
- [11] I. Sandberg, et al., "Data exploitation of new Galileo environmental monitoring units," *IEEE Trans. Nucl. Sci.*, vol. 66, no. 7, pp. 1761-1769, May 2019.
- [12] T. Nagatsuma, K. Sakaguchi, Y. Kubo, et al., "Space environment data acquisition monitor onboard Himawari-8 for space environment monitoring on the Japanese meridian of geostationary orbit," *Earth Planets Space*, vol. 69, Art. no. 75, 2017. [Online]. Available: <https://doi.org/10.1186/s40623-017-0659-6>.
- [13] K.A. Ryden, P. A. Morris, K. A. Ford, B. Taylor, C. I. Underwood, S. Jason, D. Rodgers, G. Mandorlo, G. Gatti, H. D. Evans and E. J. Daly, "Observations of internal charging currents in medium earth orbit," *IEEE Trans. Plasma Sci.*, vol. 36, no. 5, pp. 2473 – 2481, Oct. 2008.
- [14] A. Holmes-Siedle, L. Adams and G. Ensell (1991), "MOS dosimeters-improvement of responsivity," *1991 Proc. Radiation and Its Effects on Components and Systems*, La Grande-Motte, France, pp. 65-69, Sept. 1991.
- [15] L.Z. Scheick, P.J. McNulty and D.R. Roth, "Dosimetry based on erasure of floating gates in the natural radiation environments of space," *IEEE Trans. Nucl. Sci.*, vol. 45, pp. 2681-2688, Dec. 1998.
- [16] P.J. McNulty, S. Yow, L.Z. Scheick and W.G. Abdel-Kader, "Charge removal from FGMS floating gates," *IEEE Trans. Nucl. Sci.*, vol. 49, pp. 3016-3021, Dec. 2002.
- [17] P.J. McNulty, K.F. Poole, M. Crissler, J. Reneau, G. Cellere, A. Paccagnella, A. Visconti, M. Bonanomi, D. Strobel, M. Fennell and R. Perez, "Sensitivity and dynamic range of FGMS dosimeters," *Radiat. Prot. Dosimetry*, vol. 122, no. 1-4, pp. 460-462, Dec. 2006.
- [18] A. Holmes-Siedle, and L. Adams, "RADFET: a review of the use of metal-oxide-silicon devices as integrating dosimeters," *Radiation Physics and Chemistry*, vol. 28, no. 2, pp. 235-244, Jan. 1986.
- [19] D. Plattard, G. Ranchoux, L. Dusseau, G. Polge, J-R. Vaillle, J. Gasiot, J. Fesquet, R. Ecoffet and N. Iborra-Brassart, "Characterization of an integrated sensor using optically stimulated luminescence for in-flight dosimetry," *IEEE Trans. Nucl. Sci.*, vol. 49 no. 3, pp. 1322-1326, June 2002.
- [20] J-R. Vaillle, S. Ducret, K. Idri, F. Saigne, S. Matias, N. Iborra, R. Germanicus, R. Ecoffet and L. Dusseau, "Hardening of a radiation sensor based on optically stimulated luminescence," *IEEE Trans. Nucl. Sci.*, vol. 50, no. 6, pp. 2358-2362, Dec. 2003.
- [21] J-R. Vaillle, F. Ravotti, P. Garcia, M. Glaser, S. Matias, K. Idri, J. Boch, E. Lorfevre, P.J. McNulty, E. Saigne and L. Dusseau, "Online dosimetry based on optically stimulated luminescence materials," *IEEE Trans. Nucl. Sci.*, vol. 52, no. 6, pp. 2578-2582, Dec. 2005.
- [22] P. Garcia, J-R Vaillle, D. Benoit, H. Charbane, G. Berger, K. Idri, J. Boch, B. Sagnes, F. Saigne, E. Lorfevre, F. Bezerra and L. Dusseau, "Simultaneous evaluation of TID and displacement damage dose using a

- single OSL sensor," *IEEE Trans. Nucl. Sci.*, vol. 53, pp. 3713-3717, Dec. 2006.
- [23] C. Deneau, J-R Vaille, L. Dusseau, J. Mekki, P. Garcia, F. Bezerra, F. Lorfevre and R. Ecoffet, "First in-flight data analysis of displacement damage on the OSL sensor on-board CARMEN-2," *IEEE Trans. Nucl. Sci.*, vol. 58, no. 3, pp. 939-944, June 2011.
- [24] G.E. Farrell, P.J. McNulty and W.G. Abdel-Kader, "Microdosimetric analysis of proton-induced reactions in silicon and gallium arsenide," *IEEE Trans. Nucl. Sci.*, vol. 31, pp. 1073-1077, Dec. 1984.
- [25] P.J. McNulty, J.D. Kinnison, R.H. Maurer, D.R. Roth, R.A. Reed and W.G. Abdel-Kader, "Energy-deposition events measured by the CRRES PHA experiment," *IEEE Trans. Nucl. Sci.*, vol. 51, pp. 3381-3388, Dec. 2004.
- [26] J.D. Kinnison, R.H. Maurer, D.R. Roth, P.J. McNulty and W.G. Abdel-Kader, "Neutron-induced pion production in silicon-based circuits," *IEEE Trans. Nucl. Sci.*, vol. 50, pp. 2251-2255, Dec. 2003.
- [27] H.J. Barnaby, "Total-ionizing-dose effects in modern CMOS technologies," *IEEE Trans. Nucl. Sci.*, vol. 53, pp. 3103-3121, Dec. 2006.
- [28] D.R. Ball, R.D. Schrimpf and H.J. Barnaby, "Separation of ionization and displacement damage using gate-controlled lateral PNP bipolar transistors," *IEEE Trans. Nucl. Sci.*, vol. 49, pp. 3185-3190, Dec. 2002.
- [29] P.C. Adell, B. Rax, I.S. Esqueda and H.J. Barnaby, "Hydrogen limits for total dose and dose rate response in linear bipolar circuits," *IEEE Trans. Nucl. Sci.*, vol. 62, pp. 2476-2481, Dec. 2015.
- [30] A. Benedetto, H. Barnaby, C. Cook, M. Campola, and A. Tender, "BJTs in Space: Enhanced Low Dose Rate Sensitivity Experiment on the NASA Space Environment Testbed," *2021 IEEE Radiation Effects Data Workshop Proceedings*. Piscataway, NJ: IEEE Publishing, pp. 125-129, 2021.
- [31] R. L. Pease, D. G. Platteter, G. W. Dunham, J. E. Seiler, H. J. Barnaby, R. D. Schrimpf, M. R. Shanyfelt, M. C. Maher, and R. N. Nowlin, "Characterization of Enhanced Low Dose Rate Sensitivity (ELDRS) Effects Using Gated Lateral PNP Transistor Structures," *IEEE Trans. Nucl. Sci.*, vol. 51, no. 6, pp. 3773-3780, Dec. 2004.
- [32] R. L. Pease, P. C. Adell, B. G. Rax, X. J. Chen, H. J. Barnaby, K. E. Holbert, and H. P. Hjalmanson, "The Effects of Hydrogen on the Enhanced Low Dose Rate Sensitivity (ELDRS) of Bipolar Linear Circuits," *IEEE Trans. Nucl. Sci.*, vol. 55, no. 6, pp. 3169-3173, Dec. 2008.
- [33] R. N. Nowlin, R. L. Pease, D. G. Platteter, G. W. Dunham, and J. E. Seiler, "Evaluating TM1019.6 ELDRS Screening Methods Using Gated Lateral PNP Transistors," *IEEE Trans. Nucl. Sci.*, vol. 52, no. 6, pp. 2609-2615, Dec. 2005.
- [34] R. Velazco, G. Foucard and P. Peronnard, "Combining results of accelerated radiation tests and fault injections to predict the error rate of an application implemented in SRAM-based FPGAs," *IEEE Trans. Nucl. Sci.*, vol. 57, no. 6, pp. 3500-3505, Dec. 2010.
- [35] D. Coppersmith, D. B. Johnson and S. M. Matyas, "A proposed mode for triple-DES encryption," *IBM Journal of Research and Development*, vol. 40, no. 2, pp. 253-262, March 1996.
- [36] F. Lima et al., "A fault injection analysis of Virtex FPGA TMR design methodology," *2001 Proc. Radiation and Its Effects on Components and Systems*, Grenoble, France, pp. 275-282, Sept. 2001.
- [37] M. Caffrey et al., "Single-Event Upsets in SRAM FPGAs," *Proc. International Conference on Military and Aerospace Programmable Logic Devices*, p. 5, Sept. 2002.
- [38] M. Ceschia et al., "Identification and classification of single-event upsets in the configuration memory of SRAM-based FPGAs," *IEEE Trans. Nucl. Sci.*, vol. 50, no. 6, pp. 2088-2094, Dec. 2003.
- [39] C. Yui et al., "SEU mitigation testing of Xilinx Virtex II FPGAs," *2003 IEEE Radiation Effects Data Workshop Proceedings*. Piscataway, NJ: IEEE Publishing, pp. 92-97, 2003.
- [40] K. M. Siewicz et al., "Experimental Methods and Results for the Evaluation of Triple Modular Redundancy SEU Mitigation Techniques with the Xilinx Kintex-7 FPGA," *2017 IEEE Radiation Effects Data Workshop Proceedings*. Piscataway, NJ: IEEE Publishing, pp. 148-154, 2017.
- [41] M. Caffrey et al., "On-Orbit Flight Results from the Reconfigurable Cibola Flight Experiment Satellite (CFESat)," *IEEE Symposium on Field Programmable Custom Computing Machines*, pp. 3-10, April 2009.
- [42] H. Quinn et al., "On-Orbit Results for the Xilinx Virtex-4 FPGA," *2012 IEEE Radiation Effects Data Workshop Proceedings*. Piscataway, NJ: IEEE Publishing, pp. 128-135, 2012.
- [43] D. Heynderickx et al., "ESA's Space Environment Information System (SPENVIS) - A WWW interface to models of the space environment and its effects," *38th Aerospace Sciences Meeting and Exhibit*. Reno, NV: AIAA Proc., AIAA-2000-0371, Jan. 2000.
- [44] P. Calvel et al., "An empirical model for predicting proton induced upset," *IEEE Trans. Nucl. Sci.*, vol. 43, no. 6, pp. 2827-2832, Dec. 1996.
- [45] R. Possamai Bastos, M. Gorchs Picas, M. Correa Cueto, and R. Velazco, "MEO Spaceflight Results of Radiation Effects in COTS FPGA-implemented Triple Modular System," *Radiation and Its Effects on Components and Systems Conference*, Venice, Italy, Oct. 2022.